

Nanowire Perovskite Solar Cell

Jeong-Hyeok Im,^{†,‡} Jingshan Luo,[‡] Marius Franckevičius,^{‡,§} Norman Pellet,^{‡,||} Peng Gao,[‡] Thomas Moehl,[‡] Shaik Mohammed Zakeeruddin,[‡] Mohammad Khaja Nazeeruddin,[‡] Michael Grätzel,^{*,‡} and Nam-Gyu Park^{*,†}

[†]School of Chemical Engineering and Department of Energy Science, Sungkyunkwan University, Suwon 440-746, Korea

[‡]Laboratory of Photonics and Interfaces, Institute of Chemical Sciences and Engineering, School of Basic Sciences, Ecole Polytechnique Fédérale de Lausanne (EPFL), CH-1015 Lausanne, Switzerland

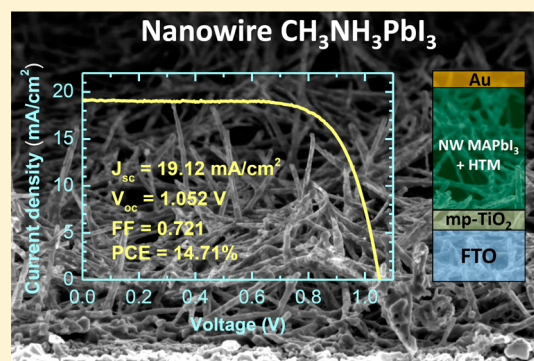
[§]Center for Physical Sciences and Technology, Savanorių Ave. 231, LT-02300 Vilnius, Lithuania

^{||}Max-Planck-Institute for Solid-State Research, Heisenbergstrasse 1, 70569 Stuttgart, Germany

S Supporting Information

ABSTRACT: Organolead iodide perovskite, $\text{CH}_3\text{NH}_3\text{PbI}_3$, was prepared in the form of nanowire by means of a small quantity of aprotic solvent in two-step spin-coating procedure. One-dimensional nanowire perovskite with the mean diameter of 100 nm showed faster carrier separation in the presence of hole transporting layer and higher lateral conductivity than the three-dimensional nanocuboid crystal. Reduction in dimensionality resulted in the hypsochromic shift of both absorption and fluorescence spectra, indicative of more localized exciton states in nanowires. The best performing device employing nanowire $\text{CH}_3\text{NH}_3\text{PbI}_3$ delivered photocurrent density of 19.12 mA/cm^2 , voltage of 1.052 V, and fill factor of 0.721, leading to a power conversion efficiency (PCE) of 14.71% at standard AM 1.5G solar illumination. A small I - V hysteresis was observed, where a PCE at forward scan was measured to be 85% of the PCE at reverse scan.

KEYWORDS: nanowire, perovskite, $\text{CH}_3\text{NH}_3\text{PbI}_3$, solar cell, aprotic solvent



Since the report on long-term durable perovskite solar cell in 2012¹ following two pioneering works on organolead halide perovskite adopted as a sensitizer in liquid junction photoelectrochemical solar cell,^{2,3} there has been a swift surge of perovskite solar cell over the years due to their low cost and superb photovoltaic performance. As a result, a power conversion efficiency (PCE) of 20.1% was certified.⁴ Methylammonium lead iodide $\text{CH}_3\text{NH}_3\text{PbI}_3$ (MAPbI₃), a key material for perovskite solar cell, can be applied to thin film p-i-n or p-n junction structure because of its balanced charge transport property^{5,6} along with micron-scale diffusion length.^{7,8} A mesoscopic pillared type with a mesoporous oxide layer and a perovskite capping layer and a planar embodiment without the mesoporous oxide layer are typical structures for perovskite solar cells,⁹ where the hole transport layer (HTL) is in contact with perovskite surface in both types. Charge transport in perovskite layer is followed by charge separation at n-type oxide/perovskite and perovskite/HTL interfaces. When considering random walk model in nanocrystalline system with grain boundaries,¹⁰ carrier transport in three-dimensional (3D) perovskite structure may not be rapid enough although carrier diffusion length reaches over 1 μm . This may affect charge separation at the n-type oxide/perovskite and the perovskite/HTL interfaces, and thereby increase recombination probability. It was found that carrier transport and recombination

were the main factors affecting photovoltaic performance, where transport rate was the same but recombination rate was faster for the mesoscopic structure.¹¹ This indicates that the dominant transport pathway is the perovskite absorber. MAPbI₃ embedded in a ZnO nanorod scaffold showed excellent external quantum efficiency over the entire wavelength,¹² which suggests that the reduced dimensionality of MAPbI₃ via the oxide nanorod template is beneficial for electron transport. However, the HTL/perovskite interfacial configuration is the same regardless of device configuration, which means that there seems to be still problem in charge separation at HTL/perovskite interface in such a layer-by-layer structure.

To improve hole migration from perovskite to HTL and separation at HTL/perovskite interface, low dimensional MAPbI₃, such as one-dimensional (1D) nanostructure, is expected to be better than 3D structure. During the course of our research on preparing 1D nanowire MAPbI₃ and studying its photovoltaic performance, similar 1D MAPbI₃ was reported.¹³ However, the reported 1D morphology was

Received: January 6, 2015

Revised: January 31, 2015

Published: February 24, 2015

produced by using a different preparation method and nanowires were tested in field emission transistors, which differ fundamentally from our photovoltaic devices. Here, we report perovskite solar cell based on nanowire MAPbI₃ that was grown by two-step spin coating technology. Without using a specific technique like electrospinning, nanowire MAPbI₃ film was surprisingly formed by coating the PbI₂ layer with an isopropanol solution of CH₃NH₃I (MAI) in the presence of small amount of polar aprotic solvent. Time-resolved fluorescence spectroscopy confirmed that charge separation at HTL/perovskite was faster for 1D nanowire than for 3D nanocube. Although the device has not been optimized, a PCE as high as 14.71% was demonstrated with nanowire MAPbI₃. To the best of our knowledge, this is the first report on nanowire perovskite solar cell to date.

Results and Discussion. Formation of MAPbI₃ Nanowires: Effect of Aprotic *N,N*-Dimethylformamide (DMF) in Isopropanol MAI Solution. The MAPbI₃ deposited on the TiO₂ layer were analyzed by field emission scanning electron microscopy (FESEM) with various morphologies. As can be seen in Figure 1, compared to the nanocubic morphology

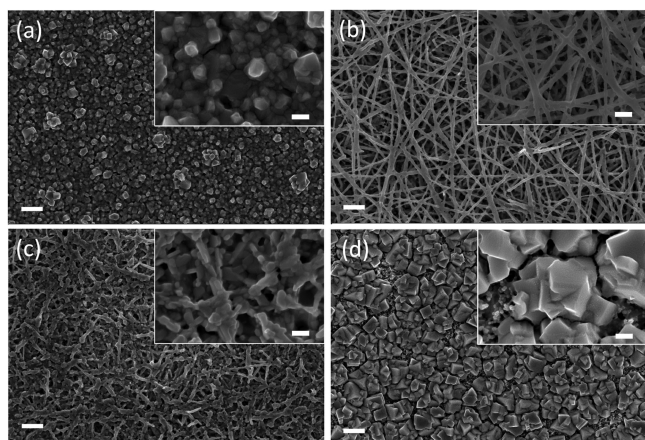


Figure 1. Plane-view SEM images of MAPbI₃ formed by two-step spin coating method using the solution of MAI in IPA (35 mg/5 mL) with (a) 10 μ L of, (b) 50 μ L of DMF, (c) 100 μ L of DMF, and (d) without DMF. MAPbI₃ was deposited on a 100 nm thick mesoporous TiO₂ (diameter of about 40 nm) layer. Scale bars represent 1 μ m (200 nm in insets).

(Figure 1d) formed by two-step spin-coating using an isopropanol solution of MAI,¹⁴ the morphology of perovskite starts to change when using a modified MAI solution with small amount of DMF in isopropanol (IPA) solution. Fused nanoparticles are formed by adding 10 μ L of DMF in the MAI isopropanol solution (Figure 1a), which is changed to nanowires as DMF increases to 50 μ L (Figure 1b). Nanowire is thickened and shortened as DMF increases further to 100 μ L (Figure 1c). Within the web of nanowires the diameters of nanowires range from \sim 30 to \sim 200 nm (Supporting Information Figure S1). Small amount of DMF is found to play a crucial role in changing 3D to 1D structure of MAPbI₃.

Formation of MAPbI₃ Nanowires: Effect of MAI Concentration. In order to explore the factors that lead to the formation of MAPbI₃ nanowire, spin-coating of the different concentration of MAI solution at the fixed amount of 50 μ L of DMF was performed. At low concentration of 0.019 M MAI solution, a less dense nanowire film is formed but its morphology looks needle shape (Figure 2a). A dense web of

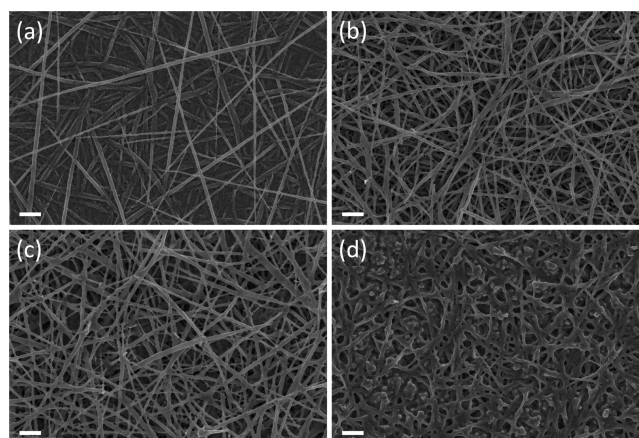


Figure 2. Plane-view SEM images of MAPbI₃ formed by two-step spin coating deposition using the 50 μ L of DMF/5 mL of IPA solution of MAI with different MAI concentration of (a) 0.019 M (15 mg MAI), (b) 0.038 M (30 mg), (c) 0.057 M (45 mg), and (d) 0.076 M (60 mg). MAPbI₃ was deposited on a 100 nm thick mesoporous TiO₂ (diameter of about 40 nm) layer. Scale bars represent 1 μ m.

nanowires is formed by the MAI solution with concentration ranging between 0.038 M (Figure 2b) and 0.057 M (Figure 2c). The vacancies in the nanowire web start to be filled as MAI concentration is higher than 0.076 M (Figure 2d and Supporting Information Figure S2). The polar aprotic solvent plays major role in structuring 1D nanowire and at the given amount of DMF the MAI concentration plays an important role in determining the porous structure of nanowires. Pore structure in the nanowire web should be taken into consideration because HTL is incorporated in the pores. The 50 μ L of DMF/5 mL of IPA solution of MAI with concentration between 0.038 M (30 mg/5 mL) and 0.057 M (45 mg/5 mL) is proposed to be an optimal condition to form a porous nanowire film.

Formation of MAPbI₃ Nanowires: Effect of Kind of Aprotic Solvents. Apart from DMF, other polar aprotic solvents were also investigated. Supporting Information Figure S3 shows the effect of different aprotic solvents, such as dimethyl sulfoxide (DMSO) and gamma butyrolactone (GBL), in the MAI solution. As observed previously, the 50 μ L of DMF in a solution of 35 mg of MAI/5 mL of IPA yields nanowires as can be seen in Supporting Information Figure S3a, whereas the same quantity of DMSO and GBL cannot lead to well-defined nanowires (Supporting Information Figure S3b and c). This implies that formability of nanowire morphology strongly depends on kind of aprotic solvents and the small quantity DMF in IPA is confirmed to play a crucial role in promoting anisotropic or 1D growth of MAPbI₃. Regarding the mechanism involved in the anisotropic growth of MAPbI₃, we postulate that the local PbI₂ in the predeposited PbI₂ solid film would be dissolved by small amount of DMF during the second spinning step. The locally dissolved PbI₂ may serve as a preferential site for reacting with MAI to grow 1D structure, like a liquid catalyst cluster model.¹⁵ On the basis of this model, GBL would not be expected to grow a 1D structure since PbI₂ is less soluble in GBL compared to DMF (we confirmed this by dissolving PbI₂ powder in GBL). On the other hand, DMSO is expected to grow nanowire because it can dissolve PbI₂, but imperfect nanowire was formed in the presence of DMSO as can be seen in Supporting Information Figure S3b. This may be related to difference in solubility between DMF and DMSO.

XRD Analysis of MAPbI₃ Nanowire. The crystal structure analysis illustrates the formation mechanism of the perovskite nanocrystals (Figure 3). Corresponding X-ray diffraction

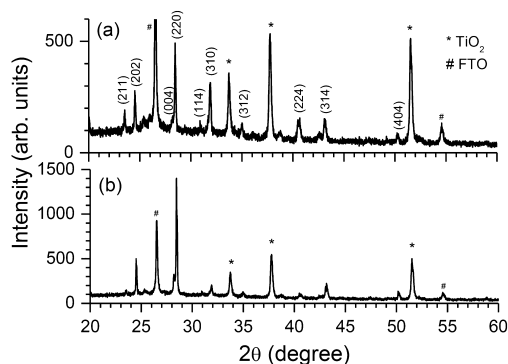


Figure 3. XRD patterns of (a) nanowire MAPbI₃ prepared from the solution of MAI in IPA (35 mg/5 mL) with 50 μ L of DMF and (b) cuboid MAPbI₃ prepared from a IPA solution of MAI without DMF.

(XRD) patterns of the polymorphic MAPbI₃ nanocrystals are shown in Figure 3b. The XRD diagram from the reference film prepared by two-step spin coating procedure without DMF¹³ is similar and match well with those of the reported tetragonal MAPbI₃ perovskite structure (space group *I4/mcm*; $a = 8.8866(3)$ Å and $c = 12.685(2)$ Å; $\alpha = \beta = \gamma = 90^\circ$).³ The corresponding SEM image (Figure 1) shows a cuboid morphology of polycrystalline MAPbI₃ with a grain size of \sim 800 nm. Analysis of the diffraction pattern of the MAPbI₃ nanowire shows a crystal structure rather similar to the cuboid shaped film with space group (*I4/mcm*) and lattice parameters of $a = 8.8586$ Å and $c = 12.628$ Å. It is noticed that the peak intensities of cuboid and nanowire perovskite nanocrystals show some differences. For example, the strongest peak (220) in cuboid particle film becomes weaker in the nanowire film, whereas the (310) peak becomes stronger, which indicates that the two films developed a quite different grain distribution. To the best of our knowledge, this type of nanowire structured MAPbI₃ architecture has not been reported previously. Preliminary Rietveld refinements also cast some further doubt on the space group *I4/mcm*:¹⁶ not only was it rather difficult to obtain truly fitting intensities, but an I-centered Bravais lattice does seem unusual for a primitive cubic cell. The solvent-controlled formation of perovskite nanowire provides an additional approach for controlling the optoelectronic properties of MAPbI₃ for optoelectronic applications perovskites in particular e solar cells.

Optoelectronic Characteristics of MAPbI₃ Nanowires. The steady-state absorption and fluorescence spectra of annealed perovskite film (FTO/TiO₂/perovskite/HTM) of different morphologies are presented in Figure 4. One can observe that measured absorption spectra show several small deviations depending on the perovskite morphology. The most obvious differences are related to their different band gaps. The absorption spectrum of nanowire perovskite is approximately 20 meV shifted toward higher energy side with respect to the absorption onset of cuboid perovskite films. The higher band gap of nanowire perovskite can be consistent with their crystal size alterations. As the average diameter of the crystals is about 100 nm and the lengths reaching one micrometer, their surface-to-volume ratio is also increased and is much larger than in the bulk. This can result in the increase in defective state that could

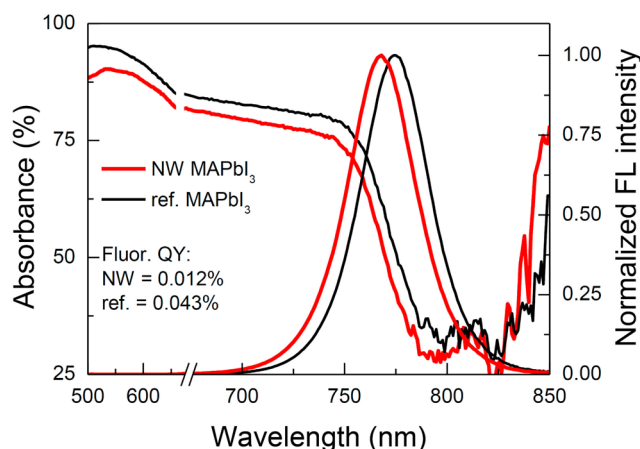


Figure 4. Absorbance and normalized fluorescence (FL) spectra of perovskite films (FTO/TiO₂/MAPbI₃/HTM) of different morphologies of the reference nanocube (black) and nanowire (red).

have an influence on the appearance of new electronic states that can affect the band gap value. It could be also seen that the shape of absorbance spectra below 600 nm slightly depends on perovskite morphology. The short wavelength absorption intensity of nanowire perovskite film is slightly lower compared to cuboid, and this can be related with its lower extinction coefficient. However, the absorbance of the perovskite films below 600 nm is very high, exceeding a value of 2. Therefore, appreciable difference can also correspond to absorbance saturation rather than to morphological differences of perovskite films. A more detailed studies on the optical properties of nanowire perovskite films need to be done. From Figure 4, we find that the photoluminescence spectra of different morphology perovskite films exhibit similar 10 nm Stokes shift. Emission maxima of bulk perovskite (cuboid) films is situated near 775 nm, whereas for nanowires, it appears at 765 nm. Because fluorescence of perovskites usually occurs due to recombination of localized excitons, the hypsochromic shift of both absorption and fluorescence spectra can be attributed to more localized exciton states in nanowires. The presence of defects can result in an increase of the trap density in the crystal accounting for the more localized nature of excitons and also band gap energy. Due to different surface defects, photoluminescence quantum yield of nanowire perovskites ($\Phi_{\text{nw}} = \sim 1.2 \times 10^{-4}$) is also slightly lower than of bulk ($\Phi_{\text{bulk}} = \sim 3.6 \times 10^{-4}$). Because titanium dioxide and hole transporting layers can extract charge carriers from perovskite, we have also performed fluorescence quenching studies in order to compare electron and hole injection efficiencies in cuboid and nanowire perovskites using films of different compositions.

Figure 5 shows fluorescence decay kinetics of perovskite films deposited on Al₂O₃ (black lines), TiO₂ (magenta) without hole transporting layer (spiro-MeOTAD), and on Al₂O₃ with HTM (green).¹⁷ Photoluminescence decays were fitted to a double-exponential decay model in order to determine relative concentrations of extracted and recombined charge carriers and their lifetimes. It is well known that free charge carrier diffusion lengths in perovskites are in the order of 100 nm to 1 μ m and this is because of long lasting electron–hole recombination in pure perovskite films. The photoluminescence lifetimes of perovskite films deposited on Al₂O₃ should reflect natural recombination events and can be also used as probes to evaluate approximate amount of recombined charges. The

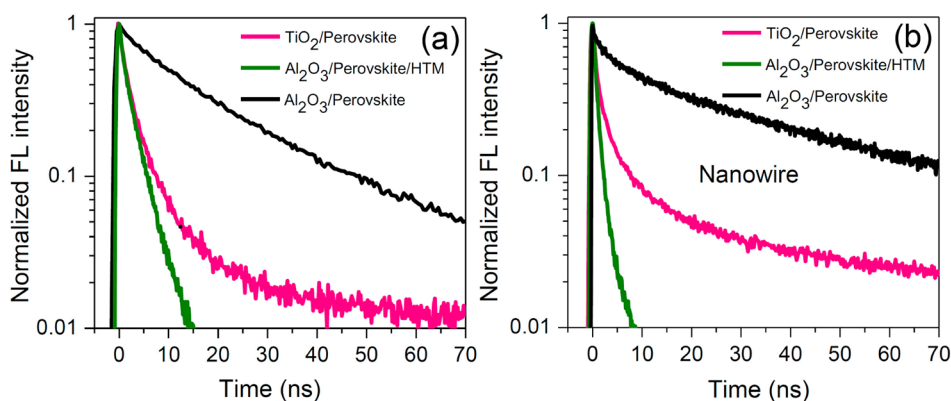


Figure 5. Normalized fluorescence (FL) decay kinetics of perovskite films of (a) the bulk (cuboid) MAPbI₃ and (b) nanowire MAPbI₃ following excitation at 406 nm.

Al₂O₃ based perovskite films show that almost 90% of charges undergo recombination with a 30 ns lifetime, whereas for nanowire perovskites, recombination represents only 78%, the carrier lifetime being about 45 ns. As we already discussed above, the presence of surface defects in nanowire perovskites is probably the main reason that could cause charge quenching before their recombination occurs. Nevertheless, although charge quenching in nanowire perovskite is more pronounced than in the bulk case; their recombination takes slightly longer. It is also important to note that when perovskite layer establishes contact with TiO₂, one can expect to have efficient electron extraction. This is the case for bulk perovskite films deposited on TiO₂ layer where about 65% of charges are extracted and remaining part undergoes recombination. It is apparent that TiO₂ is not a perfect material for electron injection, even for bulk films. However, using nanowire perovskite, there are just about 51% of charges that can be injected into TiO₂. Electron extraction of nanowire perovskite deposited on TiO₂ layer is not efficient as for bulk perovskite probably because of worse charge extraction at the interface, resulting from the poor contact with TiO₂ layer. Perovskite deposited on electron blocking layer and coated with HTM also shows some interesting features. Fluorescence quenching of nanowire perovskite is observed to be slightly faster and more efficient than in bulk case. Approximately 79% of holes are injected into HTM from nanowire perovskite with the lifetime of about 700 ps. Hole extraction in bulk perovskite films is not so efficient because just about 68% of all of the photogenerated holes are injected into HTM, the fluorescence quenching lifetime being 2.9 ns. The hole extraction from nanowire perovskite is expected to be more efficient than in the bulk case because of their increased surface area, which establishes better contact with HTM.

The DC conductivity of the in-plane nanowires was measured by evaporating two gold contacts 0.14 μm apart onto a film of perovskite deposited by two-step spin coating procedure in the presence of DMF onto a microscope slide glass. The resistance was measured under various light intensities by reversible *J*–*V* scans. Four-point probe measurements in the in line configuration were unsuccessful due to the high resistivity of the sample under low light bias. Henceforth, only the relative conductivity should be considered. We observe that the lateral conductivity of the nanowire film is enhanced by a factor 1.3 to 1.6 at high light intensities, indicating a better connectivity pathway, increasing the apparent mobility (Figure 6). At low light intensities, we observe that the conductivity of

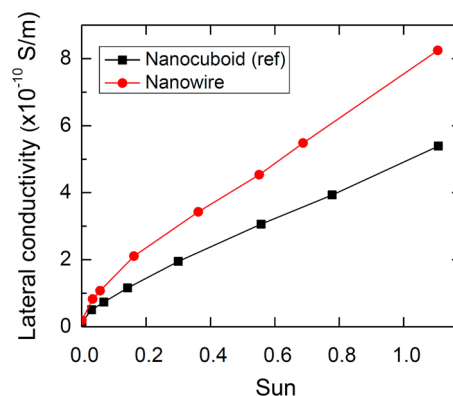


Figure 6. DC conductivity of the in-plane perovskite by evaporating two gold contacts 0.14 μm apart onto a film.

the wires is closer to the one of the standard sample, which indicates that crystal boundaries become less resistive and phenomenon such as charge trapping come into play.

Photovoltaic Performance. We fabricated perovskite solar cell based on nanowire MAPbI₃. Figure 7 shows SEM images of a full cell that is composed of FTO/compact TiO₂/mesoporous (mp)-TiO₂ + MAPbI₃/nanowire (NW) MAPbI₃ + Spiro-MeOTAD/Au. Due to partial vertical orientation of the nanowires (Supporting Information Figure S4), it is difficult to contact the top of these rods nanowires by spiro-MeOTAD. In order to improve the coverage if nanowire MAPbI₃ with spiro-MeOTAD we increased the layer thickness of spiro-MeOTAD by augmenting its concentration and reducing the spinning rate. Using this method, an average PCE of 12.62% was achieved along with short-circuit photocurrent density (*J*_{sc}) of 18.91 mA/cm², open-circuit voltage (*V*_{oc}) of 1.011 V and fill factor (FF) of 0.647. The best performing nanowire perovskite solar cell device with active area of 0.159 cm² shows *J*_{sc} = 19.12 mA/cm², *V*_{oc} = 1.052 V, and FF = 0.721, leading to a PCE of 14.71% at AM 1.5G full solar illumination (Figure 8a). The onset wavelength in EQE spectrum in Figure 8b is around 790 nm, 10 nm lower than the bulk MAPbI₃ solar cell,¹⁴ which is consistent with emission spectra shown in Figure 4. Regarding *I*–*V* hysteresis, nanowire-based perovskite solar cell exhibits a little *I*–*V* hysteresis. A PCE observed at forward scan (canning from short-circuit to open-circuit) is 85% of the PCE at reverse scan (Supporting Information Figure S5), which is, however, not as pronounced as the 3D cuboid or the planar structure.¹⁸

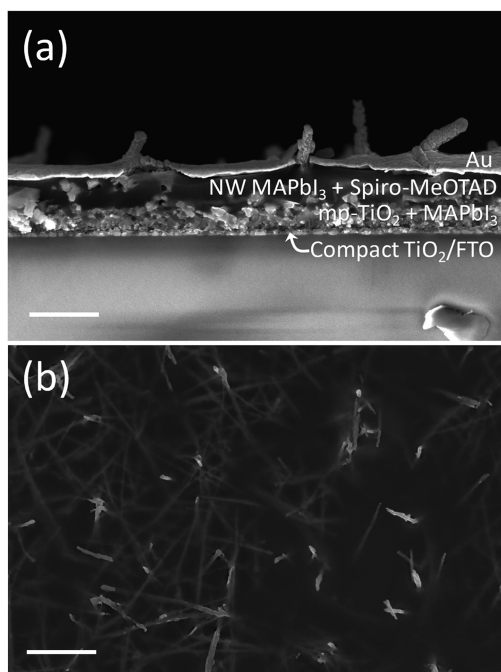


Figure 7. (a) Cross-sectional and (b) plane-view SEM images of a full cell employing MAPbI₃ nanowire. Scale bars represent 1 μ m. Full cell configuration in the cross-sectional SEM in (a) is FTO/compact TiO₂/mesoporous (mp)-TiO₂ + MAPbI₃/nanowire (NW) MAPbI₃ + Spiro-MeOTAD/Au.

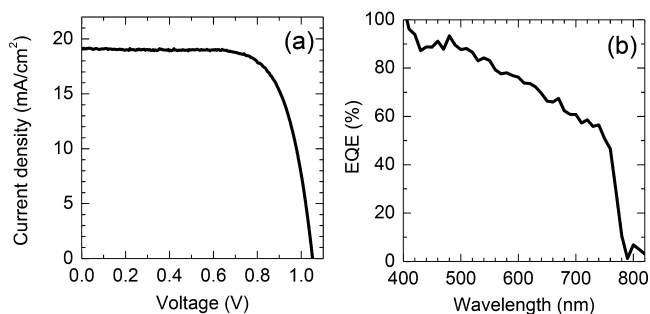


Figure 8. (a) Current–voltage curve measured at AM 1.5G illumination with light intensity of 98.6 mW/cm² and (b) external quantum efficiency (EQE) of perovskite solar cell based on MAPbI₃ nanowire.

Because the device fabrication is not optimized, we anticipate further improvement based on our optoelectronic observations.

Conclusions. Nanowire perovskite solar cell with a PCE of 14.71% was fabricated for the first time. Nanowire MAPbI₃ with the mean diameter of 100 nm was successfully grown with the aid of aprotic solvent DMF in two-step spin coating procedure. Compared to the bulk MAPbI₃, hole injection from perovskite to spiro-MeOTAD was improved for nanowire structure, which give important new insight into the engineering at perovskite/HTL interface. The lateral conductivity of nanowire film was higher than that of bulk cuboid film. Because charge separation and conductivity is better in nanowire structure, higher photovoltaic performance is expected in case that flat web structured nanowire film is fabricated.

Materials and Methods. *Nanowire Perovskite Solar Cell Fabrication.* FTO glasses (Nippon Sheet Glass) were cleaned in an ultrasonic bath containing ethanol for 30 min. A compact TiO₂ blocking layer was spin-coated on a FTO glass at 2000

rpm for 30 s using 0.15 M solution of titanium diisopropoxide bis(acetylacetonate) (75 wt % in isopropanol, Aldrich) in 1-butanol (99.8%, Aldrich), which was heated at 125 °C for 5 min. After cooling down to room temperature, the TiO₂ paste (ca. 40 nm-sized TiO₂ particles) was spin-coated at 2000 rpm for 10 s, in which the pristine paste was diluted in ethanol (0.1 g/mL). After drying at 100 °C for 5 min, the film was annealed at 550 °C for 30 min, which led to thickness of about 100 nm. The mesoporous TiO₂ film was immersed in 0.02 M aqueous TiCl₄ (>98%, Aldrich) solution at 70 °C for 30 min. After washing with deionized water and drying, the film was heated again at 500 °C for 30 min. MAPbI₃ nanowire was formed using two-step spin-coating procedure. To deposit PbI₂ layer, 1 M PbI₂ solution was prepared by dissolving 462 mg PbI₂ (99%, Aldrich) in 1 mL of DMF (99.8%, Sigma-Aldrich) at 70 °C. Then, 20 μ L of PbI₂ solution was loaded on the substrate for 10 s, which was spun at 3000 rpm for 5 s and 6000 rpm for 5 s. After that, 200 μ L of the solution of MAI in isopropanol (35 mg/5 mL) including 50 μ L of DMF was loaded on the PbI₂-coated substrate for 40 s, which was spun at 4000 rpm for 20 s and dried at 100 °C for 5 min. Then, 30 μ L of (2,2',7,7'-tetrakis(*N,N*-di-*p*-methoxyphenylamine)-9,9-spirobifluorene) (spiro-MeOTAD) solution was spin-coated on the MAPbI₃ nanowire film at 2000 rpm for 10 s. A spiro-MeOTAD solution was prepared by dissolving 122.5 mg of spiro-MeOTAD in 1 mL of chlorobenzene, to which 28.8 μ L of 4-*tert*-butylpyridine, 17.5 μ L of lithium bis(trifluoromethanesulfonyl)imide (Li-TFSI) solution (520 mg in 1 mL of acetonitrile (Sigma-Aldrich, 99.8%)), and 21.9 μ L of tris(2-(1H-pyrazol-1-yl)-4-*tert*-butylpyridine)cobalt(III) bis(trifluoromethylsulfonyl)imide solution (400 mg in 1 mL acetonitrile) were added. Finally, 80 nm of gold was thermally evaporated on the spiro-MeOTAD coated film.

Device Characterizations. The solar cells were measured using a 450 W xenon light source (Oriel) with an irradiance of 100 mW/cm². A Schott K113 Tempax filter (Präzisions Glas & Optik GmbH) was used to reduce the spectral mismatch between AM 1.5G and the simulated illumination to ~4% between 350 and 750 nm. Photocurrent density (*J*) and voltage (*V*) characteristics of the devices were obtained by applying an external voltage bias while measuring the current response with a source meter (Keithley 2400). The voltage step and equilibration times were 10 mV and 200 ms, respectively. The cells were covered with a black mask having an aperture area of 0.159 cm². EQE spectra were recorded as functions of wavelength in the alternating current (AC) mode under a constant white light bias of ~10 mW/cm², supplied by an array of white-light-emitting diodes. The excitation beam coming from a 300 W xenon lamp (ILC Technology) was focused through a Gemini-180 double monochromator (Jobin Yvon) and chopped at ~2 Hz. The signal was recorded using a Model SR830 DSP lock-in amplifier (Stanford Research Systems). All measurements were conducted using a nonreflective metal aperture of 0.159 cm² to define the active area of the device and avoid light scattering through the sides.

Structure and Morphology Characterizations. The plane-view and cross-sectional morphologies of the perovskite solar cell was characterized using a high-resolution scanning electron microscope (ZEISS Merlin). The layer of perovskite on the TiO₂ film was deposited using two-step spin coating procedure. X-ray powder diagrams were recorded on an X'Pert MPD PRO (Panalytical) equipped with a ceramic tube (Cu anode, λ = 1.54060 Å), a secondary graphite (002) monochromator, and a

RTMS X'celerator (Panalytical). The measurements were done in the Bragg–Brentano geometry. The samples were mounted without further modification and the automatic divergence slit and beam mask were adjusted to the dimension of the films. A step size of 0.008° was chosen for an acquisition time of 7.5 min/degree.

Optoelectronic Characterizations. Optical absorption spectra of perovskite films were recorded with a CARY-5 UV–vis–NIR spectrophotometer in transmission mode, whereas for absorbance and fluorescence quantum yield measurements, spectrofluorometer Fluorolog 322 (Horiba Jobin Yvon Ltd.), equipped with 102 mm diameter integrating sphere (Horiba F-3018) was used. Absorbance spectra of samples measured in transmittance and diffuse reflectance geometry, that is, at 0° and 90° , respectively, to the sample illumination with 450 W xenon lamp, were then evaluated by subtracting total transmittance from unity. Photoluminescence quantum yield was determined by measuring light source emission and perovskite film photoluminescence, following and without sample illumination. Photoluminescence quantum yield of perovskite films was calculated according to methodology reported elsewhere.¹⁹

Fluorescence spectra and fluorescence decay kinetics were recorded with spectrofluorometer Fluorolog 322 working in single-photon counting mode. Picosecond pulsed diode laser head NanoLED-40SLH (Horiba) emitting 200 ps duration pulses at 406 nm with repetition rate of 1 MHz was used for samples excitation. The used excitation energy was about 11 pJ/pulse. Fluorescence spectrum was corrected for the instrument response function. The maximum reached time resolution of the setup was about several hundred picoseconds by applying apparatus function deconvolution.

Conductivity Measurements. To measure the in-plane DC conductivity of the samples, we deposited perovskite by two step spin coating procedure over microscope slide glass. Gold contacts were evaporated 140 μm apart of each other. The conductivity was measured by a Keithley SMU 2612B sourcemeter in four-wire measurement mode by recording J – V scans between -1 and $+1$ V. The resistance was determined from the slope of the J – V traces. The samples were illuminated by a 10×10 array of Luxeonstar Cool White 5650K LEDs. The LEDs were calibrated using a commercial silicon photodiode. No solar spectrum mismatch correction was applied.

■ ASSOCIATED CONTENT

📄 Supporting Information

Plane-view SEM image of nanowire MAPbI_3 formed by two-step spin coating method using the solution of MAI in 5 mL of IPA and 50 μL of DMF, plane-view SEM images of MAPbI_3 formed by two-step spin coating deposition using the 50 μL of DMF/5 mL of IPA solution of MAI with different MAI amount, plane-view SEM images of MAPbI_3 formed by two-step spin coating method using a IPA solution of MAI (35 mg/5 mL) with different aprotic medium, 3D-view SEM image of MAPbI_3 formed by two-step spin coating method using the 50 μL of DMF/5 mL of IPA solution of MAI (35 mg), and J – V curves of nanowire perovskite solar cell depending on scan direction. This material is available free of charge via the Internet at <http://pubs.acs.org>.

■ AUTHOR INFORMATION

Corresponding Authors

*E-mail: michael.graetzel@epfl.ch. Tel.: +41-21-693-3112. Fax: +41-21-693-6100.

*E-mail: npark@skku.edu. Tel.: +82-31-290-7241. Fax: +82-31-290-7272.

Notes

The authors declare no competing financial interest.

■ ACKNOWLEDGMENTS

J.H.I. and N.G.P. acknowledges financial support by the National Research Foundation of Korea (NRF) grants funded by the Ministry of Science, ICT & Future Planning (MSIP) of Korea under contracts No. NRF-2010-0014992, NRF-2012M1A2A2671721, NRF-2012M3A7B4049986 (Nano Material Technology Development Program), and NRF-2012M3A6A7054861 (Global Frontier R&D Program on Center for Multiscale Energy System). M.G. acknowledges financial support by the Swiss National Science Foundation and the European Research Council through the Advanced Research Grant (ARG no. 247404). M.K.N. and M.G. acknowledge financial support by the European FP7 project NANOMATCELL (Grant 308997). M.F. acknowledges a Scienc fellowshp under Project Code 13.194.

■ REFERENCES

- (1) Kim, H.-S.; Lee, C.-R.; Im, J.-H.; Lee, K.-B.; Moehl, T.; Marchioro, A.; Moon, S.-J.; Humphry-Baker, R.; Yum, J.-H.; Moser, J.-E.; Grätzel, M.; Park, N.-G. *Sci. Rep.* **2012**, *2* (591), 1–7.
- (2) Kojima, A.; Teshima, K.; Shirai, Y.; Miyasaka, T. *J. Am. Chem. Soc.* **2009**, *131*, 6050–6051.
- (3) Im, J.-H.; Lee, C.-R.; Lee, J.-W.; Park, S.-W.; Park, N.-G. *Nanoscale* **2011**, *3*, 4088–4093.
- (4) Best Research-Cell Efficiencies. http://www.nrel.gov/ncpv/images/efficiency_chart.jpg (accessed Feb 2015).
- (5) Xing, G.; Mathews, N.; Sun, S.; Lim, S. S.; Lam, Y. M.; Grätzel, M.; Mhaisalkar, S.; Sum, T. C. *Science* **2013**, *342*, 344–347.
- (6) Stranks, S. D.; Eperon, G. E.; Grancini, G.; Menelaou, C.; Alcocer, M. J. P.; Leijtens, T.; Herz, L. M.; Petrozza, A.; Snaith, H. J. *Science* **2013**, *342*, 341–344.
- (7) Edri, E.; Kirmayer, S.; Henning, A.; Mukhopadhyay, S.; Gartsman, K.; Rosenwaks, Y.; Hodes, G.; Cahen, D. *Nano Lett.* **2014**, *14*, 1000–1004.
- (8) Zhao, Y.; Nardes, A. M.; Zhu, K. *J. Phys. Chem. Lett.* **2014**, *5*, 490–494.
- (9) Kim, H.-S.; Im, S. H.; Park, N.-G. *J. Phys. Chem. C* **2014**, *118*, 5615–5625.
- (10) Nelson, J. *J. Phys. Rev. B* **1999**, *59*, 15374–15380.
- (11) Gonzalez-Pedro, V.; Juarez-Perez, E. J.; Arsyad, W.-S.; Barea, E. M.; Fabregat-Santiago, F.; Mora-Sero, I.; Bisquert, J. *Nano Lett.* **2014**, *14*, 888–893.
- (12) Son, D.-Y.; Im, J.-H.; Kim, H.-S.; Park, N.-G. *J. Phys. Chem. C* **2014**, *118*, 16567–16573.
- (13) Horvath, E.; Spina, M.; Szekrényes, Z.; Kamaras, K.; Gaal, R.; Gachet, D.; Forro, L. *Nano Lett.* **2014**, *14*, 6761–6766.
- (14) Im, J.-H.; Jang, I.-H.; Pellet, N.; Grätzel, M.; Park, N.-G. *Nat. Nanotechnol.* **2014**, *9*, 927–932.
- (15) Hu, J.; Odom, T. W.; Lieber, C. *Acc. Chem. Res.* **1999**, *32*, 435–445.
- (16) Liu, M.; Johnston, M. B.; Snaith, H. J. *Nature* **2013**, *501*, 395–398.
- (17) Wang, J. T.-W.; Ball, J. M.; Barea, E. M.; Abate, A.; Alexander-Webber, J. A.; Huang, J.; Saliba, M.; Mora-Sero, I.; Bisquert, J.; Snaith, H. J.; Nicholas, R. J. *Nano Lett.* **2014**, *14*, 724–730.
- (18) Kim, H.-S.; Park, N.-G. *J. Phys. Chem. Lett.* **2014**, *5*, 2927–2934.

(19) de Mello, J. C.; Wittmann, H. F.; Friend, R. H. *Adv. Mater.* **1997**, *9*, 230–232.